Assessment of Hydrogen Accumulation Behavior in Al-Zn-Mg Alloy under Strain with Kelvin Force Microscopy

Fujihara, Hiro
Department of Mechanical Engineering, Kyushu University

Toda, Hiroyuki
Department of Mechanical Engineering, Kyushu University

Arita, Makoto
Department of Mechanical Engineering, Kyushu University

Shimizu, Kazuyuki
Department of Mechanical Engineering, Kyushu University

他

出版情報：MATERIALS TRANSACTIONS. 62 (5), pp.636-641, 2021-05-01. 日本金属学会
バージョン：

Materials Transactions, Vol. 62, No. 5 (2021) pp. 636 to 641

Assessment of Hydrogen Accumulation Behavior in Al–Zn–Mg Alloy under Strain with Kelvin Force Microscopy

Hiro Fujihara[1,*], Hiroyuki Toda[1], Makoto Arita[2], Kazuyuki Shimizu[3], Akihisa Takeuchi[4] and Kentaro Uesugi[4]

[1]*Department of Mechanical Engineering, Kyushu University, Fukuoka 819-0395, Japan*
[2]*Department of Materials Science and Engineering, Kyushu University, Fukuoka 819-0395, Japan*
[3]*Department of Physical Science and Materials Engineering, Iwate University, Morioka 020-8551, Japan*
[4]*Japan Synchrotron Radiation Research Institute, Hyogo 679-5198, Japan*

Hydrogen embrittlement in aluminum alloys occurs due to local hydrogen accumulation during deformation. Investigating hydrogen diffusion with plastic deformation can help researchers further understand hydrogen embrittlement behavior in terms of its occurrence condition. We assessed hydrogen accumulation behavior in Al–Zn–Mg alloys under strain by combining tensile testing with Kelvin force microscopy. Additionally, the effects of microstructures on hydrogen accumulation were analyzed in detail. Hydrogen accumulated around specific grain boundaries, and it was likely that accumulated hydrogen was repartitioned to the generated vacancies, due to deformation, and the precipitate interfaces. [doi:10.2320/matertrans.L-M2020873]

(Received September 1, 2020; Accepted November 19, 2020; Published April 25, 2021)

Keywords: *hydrogen embrittlement, aluminum alloys, Kelvin force microscopy, hydrogen accumulation*

1. Introduction

Several mechanisms have been proposed for quasi-cleavage fracture, which is one of the hydrogen embrittlement fracture modes. Neeraj *et al.* have reported a mechanism in which quasi-cleavage fractures occur due to hydrogen accumulation and the localization of dislocation ahead of the crack tip.[1)] Zhang *et al.* have proposed another mechanism in which quasi-cleave fractures originate from void nucleation at the intersection of slip bands and then propagate along the slip planes with the highest Schmid factor.[2,3)] As in these reports, it has been generally believed that dislocations are involved in the occurrence of quasi-cleavage fracture.

Several recent studies have investigated quasi-cleavage fractures in Al–Zn–Mg alloys. Hirayama *et al.* have revealed that quasi-cleavage cracks propagate regardless of the crystal orientation, and they asserted that dislocations did not contribute to the occurrence of quasi-cleavage fractures.[4)] Tsuru *et al.* have investigated the interaction of hydrogen and the interface between aluminum and $MgZn_2$ precipitates through first-principles calculations.[5)] They have revealed that the precipitate interface spontaneously debonds when the hydrogen concentration at the interface reaches approximately 10^{26} atoms H/m^3 and proposed this as a new mechanism of quasi-cleavage fracture. However, even in a specimen that has been precharged with hydrogen, the hydrogen concentration at the interface is only approximately 10^{24} atoms H/m^3, which is 100 times lower than this debonding criterion.[6)] Therefore, hydrogen should locally accumulate ahead of the crack tip during deformation for hydrogen embrittlement to occur. Investigating the temporal evolution of hydrogen diffusion with plastic deformation can help researchers further understand the hydrogen embrittlement behavior in aluminum alloys.

The most effective method to elucidate hydrogen diffusion behavior is the direct observation of changes in the distribution of hydrogen. In addition, a high spatial resolution is needs to observe local hydrogen diffusion behavior. The hydrogen microprint technique and secondary ion mass spectrometry have been used to identify hydrogen trapping sites and observe hydrogen segregation at grain boundaries.[7–11)] In addition to these methods, the atom probe technique has enabled Takahashi *et al.* to visualize the hydrogen distribution in three dimensions.[12)] However, these methods cannot enable in-situ observations of change in the local hydrogen distribution.

Senöz *et al.* have succeeded in indirectly observing the temporal changes in the distribution of the surface hydrogen concentration on palladium and dual-phase steel membranes with microscale spatial resolution by employing Kelvin force microscopy (KFM).[13)] Evers *et al.* have also reported that the surface potential decreases with an increase in the hydrogen concentration on the surface of Pd.[14)] In addition, Larignon *et al.* have revealed that the surface potential also decreases due to the existence of hydrogen within the detectability of KFM in a 2024 aluminum alloy.[9,15)] This measurement technique provides surface topography and surface potential images with a submicron spatial resolution and is expected to be applied to in-situ tensile tests.

In the present study, we attempted to observe the temporal changes in the hydrogen distribution in an Al–Zn–Mg alloy under tensile strain by combining tensile tests with KFM. In addition to aluminum samples, preliminary investigations were conducted for palladium, which has a considerably higher hydrogen solubility than aluminum alloys, to more clearly confirm the effects of hydrogen on surface potential. Additionally, the microstructure and three-dimensional strain distribution, which are factors that affect hydrogen diffusion, were obtained using scanning electron microscopy (SEM)/electron backscatter diffraction (EBSD) and X-ray microtomography (XMT). The effects of these

*Graduate Student, Kyushu University. Corresponding author, E-mail: fujihara.hiro.361@s.kyushu-u.ac.jp

factors on the change in hydrogen distribution were assessed.

2. Experimental Procedure

Pure palladium (99.5% purity) and a modified 7150 aluminum alloy with chemical composition of Al–10.0Zn–2.40Mg–1.50Cu–0.15Zr–0.04Ti–0.05Si–0.05Fe (mass%) were used in the present study. The palladium sample was prepared by recrystallization treatment (1173 K for 1 h) in vacuum. Then, hydrogen was charged in the palladium sample by employing electrolytic charging. This hydrogen charging was performed at room temperature using a platinum anode in a 0.1 mol/L H_2SO_4 solution at a current density of 10 A/m^2. The aluminum sample was prepared by homogenization (743 K for 24 h), hot rolling (673 K), solution treatment (748 K for 2 h) and aging treatment (393 K for 6 h and 423 K for 5 h). Specimen of aluminum for the in-situ tensile tests were prepared by employing electrical discharge machining (EDM) in water. The gauge length and cross-sectional area of the specimen were 0.7 mm and 0.6 mm × 0.6 mm, respectively; these dimensions are the same as those in a previous report.[6)]

We measured the hydrogen concentration in the specimens with thermal desorption analysis (TDA, PDHA-1000, NISSHA FIS, Inc.). The thermal desorption curve was obtained by heating from room temperature to 873 K for the palladium sample and to 773 K for the aluminum sample at a heating rate of 1.5 K/min.

An in-situ tensile test for the aluminum sample with XMT observation was carried out at BL20XU in SPring-8. A monochromatic X-ray beam with an X-ray energy of 20 keV was used. A total of 1800 transmission images were captured in 0.1° increments over a range of 180°. Seven scans were performed while holding an applied strain for 8.9 min at each tensile step. The applied strain levels were 0.0, 1.9, 3.7, 5.7, 7.7, 10.2, and 12.9%. Three-dimensional images were reconstructed from the obtained transmission images using the convolution back-projection algorithm.

KFM measurements were carried out with an Agilent 5400 scanning probe microscope in a nitrogen gas atmosphere. The palladium sample after hydrogen charging was polished with emery paper followed by polishing with a colloidal silica solution. Then, KFM measurements were obtained for the specimen surface. The aluminum sample after in-situ observation with XMT was polished under the same conditions as those for the palladium sample. After applying an additional tensile strain to the polished aluminum sample, the KFM measurements were obtained for the specimen surface. According to the Nernst equation, the surface potential decreases with an increase in hydrogen concentration.[14)] However, there is no quantitative relationship between the hydrogen concentration and the surface potential. To assess the hydrogen accumulation behavior, surface potential images were taken twice in the same region. The second measurement was performed 10 min after the first measurement. Subtraction between the couple of the surface potential images can eliminate the influence of the surface topography and grain boundary, which are some of the factors that influence the surface potential. The remaining factor (i.e., surface potential change due to corrosion) can be precisely evaluated by observing the change in the topography.

The three-dimensional strain distribution in the region in which the KFM measurements were obtained was calculated based on the physical displacement of the intermetallic particles that existed within 14 µm in the depth direction from the KFM measurement surface.[16)] To map the grain boundaries and measurements of crystal misorientation, EBSD analysis was performed using a TSL EBSD system and a Hitachi SU6600 instrument.

3. Results and Discussions

3.1 Preliminary investigation using pure palladium

Figure 1 shows the hydrogen desorption curves of the hydrogen-charged palladium and aluminum samples. The hydrogen concentration in the palladium sample were 593 and 119 mass ppm when observed 1 and 31 h after hydrogen charging, respectively; these values were approximately 20–90 times higher than the aluminum sample used, as shown in Fig. 1(a).

KFM measurements were conducted 4.5, 7.6, and 24.3 h after hydrogen charging. Figure 2 shows the surface topography and potential images at each time along with the change in surface potential over time. Figure 3 shows the surface potential profiles along section a-a′, which is shown as black solid line in Fig. 2(d)–(f). It was revealed that the

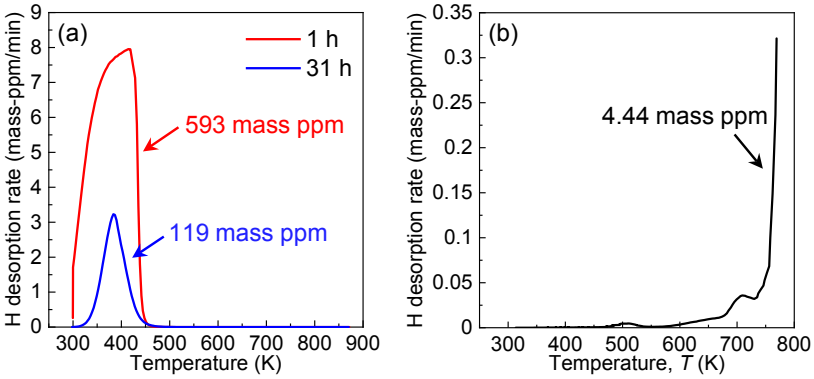

Fig. 1 Thermal desorption curves of the (a) palladium and (b) aluminum samples measured at a heating rate of 1.5 K/min. The tests for the palladium samples were performed 1 and 31 h after hydrogen charging. The test for the aluminum sample was performed after EDM.

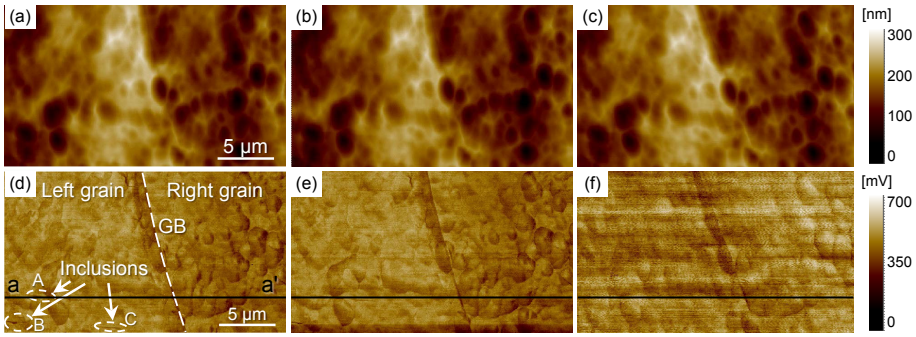

Fig. 2 (a)–(c) Surface topography and (d)–(f) surface potential images for the pure palladium sample obtained by employing KFM, which were taken (a), (d) 4.5, (b), (e) 7.6, and (c), (f) 24.3 h after hydrogen charging.

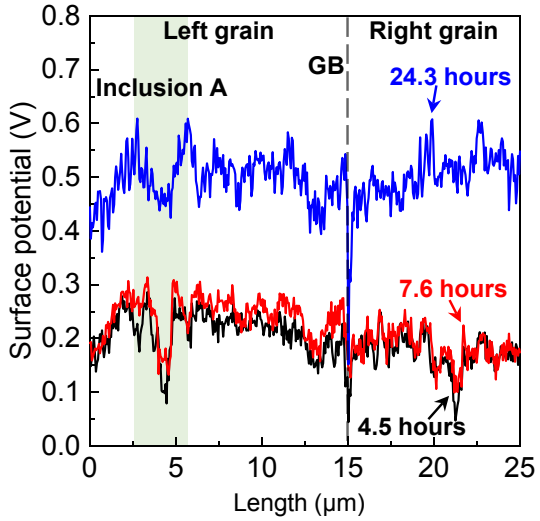

Fig. 3 Line profiles of the surface potential along section a-a′, which is shown as the black solid lines in Fig. 2.

surface potential clearly increased in both grain interiors over time. Therefore, from the TDA and KFM measurement results, it was confirmed that the surface potential clearly increased in the palladium sample with the decrease in hydrogen concentration over time.

3.2 XMT and KFM measurements for aluminum alloy

The measured hydrogen concentration in the aluminum sample after EDM was 4.44 mass ppm, as shown in Fig. 1(b). Since the measurement should be truncated at 773 K in this thermal desorption analysis, the actual total hydrogen concentration would be higher than this value. The present authors have measured the total hydrogen concentration of the same material (same lot) that had been thermomechanically treated and EDM-processed through processes identical to this study by employing the vacuum fusion method; thus, the total hydrogen concentration could be measured precisely.[17] The measured hydrogen concentration was 6.97 mass ppm.[17] It is therefore reasonable to assume that hydrogen desorption between 773 K and the melting point would amount to approximately 2.5 mass ppm for the aluminum sample used in the present study.

A quasi-cleavage crack initiated at an applied strain of 1.9% and grew to a length of 40 μm at an applied strain of 12.8%. Thereafter, the aluminum sample was unloaded and then reloaded to achieve a plastic strain of approximately 4% for the in-situ KFM measurements. The KFM measurements were conducted ahead of the crack tip while holding the applied displacement. Figure 4 shows the morphology of the specimen surface around the quasi-cleavage crack. A SEM image of the surface after strain application is shown in Fig. 4(a). The KFM measurements were difficult at the crack tip because there were large surface undulations. Therefore, measurements were conducted in regions A and B, which were 135 and 75 μm ahead of the crack tip, respectively, as shown in Fig. 4(a). The measurement in region A was taken 30 min after applying strain, and the measurement in region B was taken 180 min after applying strain. Figure 4(b) and (c) shows the surface topography images from the first and second measurements in region A, in which slip bands formed by deformation were observed. Comparing these two images indicated that there was no change in the surface topography. Figure 5 shows the surface potential images, which were measured at the same time as the surface topography, and an inverse pole figure (IPF) map was obtained using the EBSD analysis in each region. A low surface potential was measured along the grain boundaries, and this value changed over time.

The surface potential was influenced not only by hydrogen but also by corrosion, the surface topography and the presence of grain boundaries. Figure 4(b) and (c) show the absence of temporal changes in the surface topography and grain boundary morphology, implying that corrosion did not occur during these measurements. As has been described, the effects of the surface topography and presence of grain boundaries were eliminated by subtracting two consecutive surface potential images. Therefore, the changes in the surface potential were only attributed to the temporal changes in the hydrogen concentration. The temporal change in surface potential was evaluated in two regions, which are highlighted within regions A and B, as shown in Fig. 5. Figure 6 shows the differences in the surface potential in the four regions. The surface potential tended to increase in region A, which was away from the crack tip, whereas the surface potential tended to decrease in region B, which was close to the crack tip. In addition, the surface potential changed especially along the grain boundaries, and the amplitude of the change in the surface potential was different at each grain boundary. The black arrows point to the grain

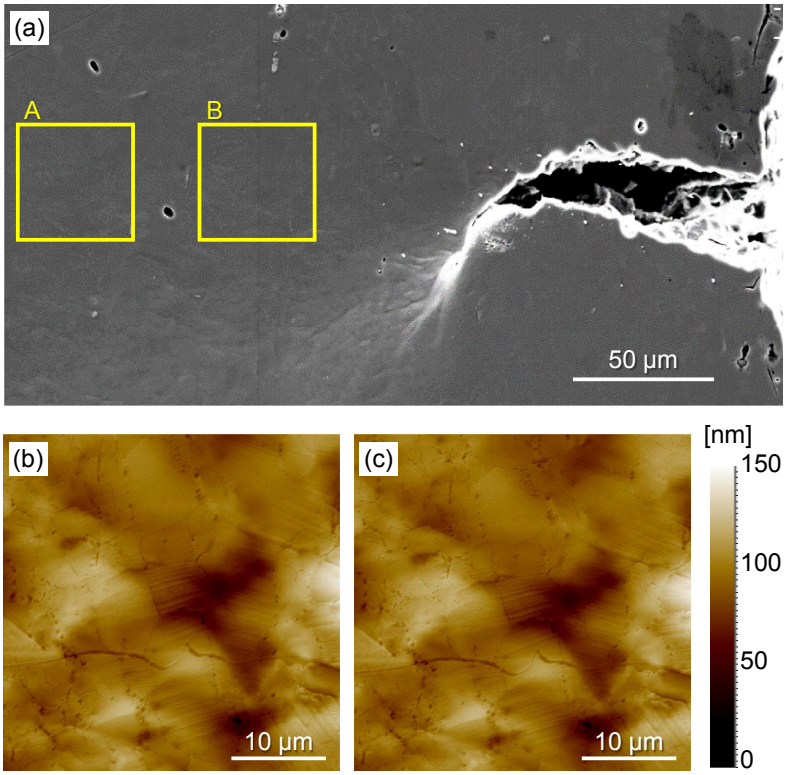

Fig. 4 (a) A SEM image captured after applying an additional 4% strain. Surface topography images of region A, which is 135 μm ahead of the crack tip (this region is highlighted in (a)), were taken (b) 30 and (c) 40 min after applying the 4% strain.

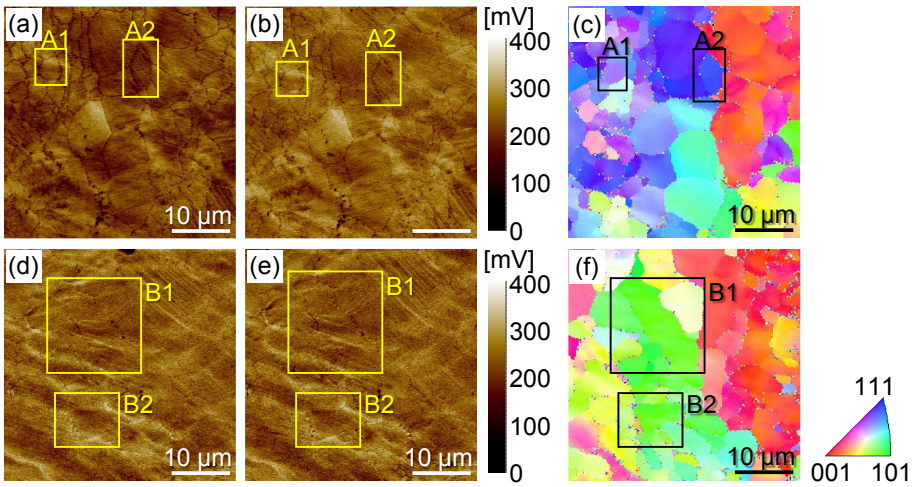

Fig. 5 Region A: surface potential images obtained by the (a) first and (b) second KFM measurements and (c) IPF map. Region B: surface potential images obtained by the (d) first and (e) second KFM measurements and (f) IPF map.

boundaries at which the change was particularly clear. Therefore, hydrogen diffused to the crack tip and accumulated around specific grain boundaries while the applied displacement was held.

3.3 Effect of the mechanical and microstructural factors on hydrogen accumulation

We discuss the factors of the hydrogen accumulation behavior observed in the present study. First, we focused on mechanical factors. The gradient of hydrostatic stress is known to act as one of the driving forces of hydrogen diffusion, and hydrogen diffuses from a low hydrostatic stress field to a high hydrostatic stress field. This type of diffusion facilitates the accumulation of hydrogen at the crack tip.

Then, we focused on microstructural factors. Compared with the EBSD analysis, which is shown in Fig. 5(c) and (f), and the hydrogen accumulation behavior, which is shown in Fig. 6, the presence of crystal misorientation did not have an effect on the hydrogen distribution. In addition, changes in the distribution of hydrogen concentration also depend on the distribution of hydrogen trapping sites. When the number of trapping sites was locally increased by deformation, the hydrogen concentration increases because hydrogen is repartitioned there. Therefore, the effect of an increased

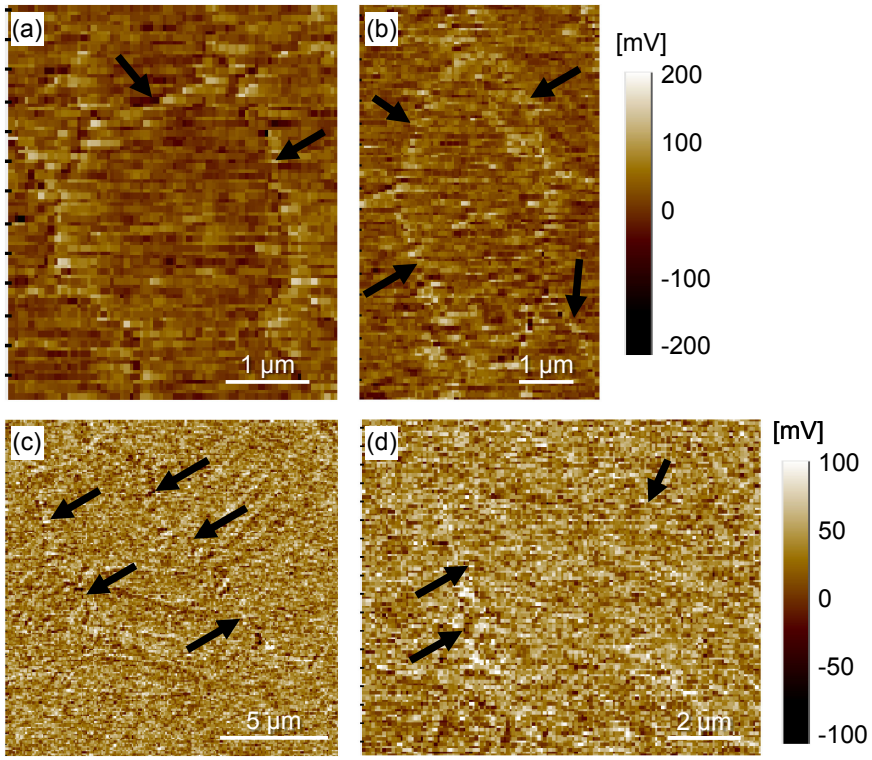

Fig. 6 Difference in the surface potential between the first and second measurements in four extracted regions, (a) A1, (b) A2, (c) B1, and (d) B2 (these regions are highlighted in Fig. 5(a) and (d)). Note that (c) and (d), which have subtle contrasts, are clearer in the electric version.

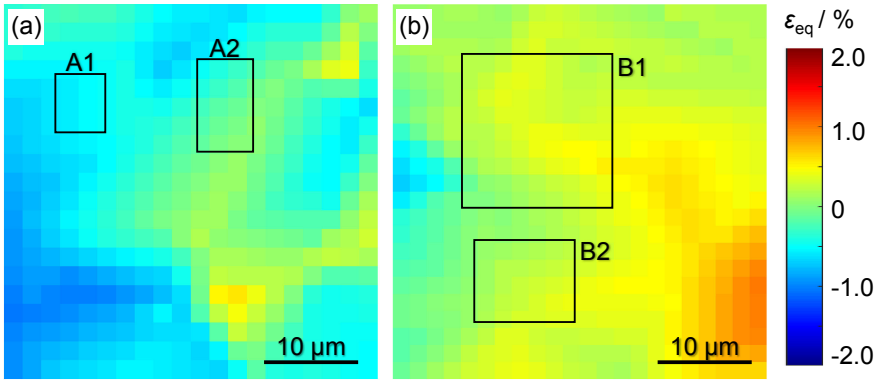

Fig. 7 Equivalent strain distribution during the in-situ tensile test obtained from XMT measurements in the same regions as the KFM measurements: (a) region A and (b) region B.

number of trapping sites on hydrogen accumulation was investigated. The number of vacancies and dislocations, which are trapping sites that increase in number during a tensile test, can be estimated from the plastic strain distribution.[6,18–21] Therefore, we qualitatively evaluated the increased number of these trapping sites by the three-dimensional plastic strain distribution. Figure 7 shows the equivalent strain distribution in the same region as the KFM measurements, and the two highlighted frames within each image correspond to the regions shown in Fig. 5(a) and (d). The change in hydrogen concentration was particularly clear in the region in which the equivalent plastic strain was relatively high. In the localized deformation region, it was reported that the number of vacancies increased approximately 10^4 times while that of dislocations increased approximately several times due to deformation.[6,22] In addition, the hydrogen binding energy of dislocation is 16.4 kJ/mol, and this value is relatively low for the trapping sites in aluminum.[23] Since the binding energy of vacancies is 28 kJ/mol and higher than the value for dislocation, the accumulated hydrogen is preferentially repartitioned to vacancy.[24] Therefore, hydrogen was repartitioned to the generated vacancies in the localized deformation region.

The increase in the hydrogen concentration depended on the distribution of the equivalent plastic strain, which was easily observed in region B1, in which hydrogen accumulated around the grain boundaries. Therefore, hydrogen accumulation behavior around grain boundaries was thought to be caused by the increase in vacancies around specific grain boundaries. Toda *et al.* have performed a three-dimensional analysis of the effect of crystallographic factors on the strain distribution.[25] They revealed that a high

equivalent strain was localized around the grain boundaries when the differences in the Taylor factor between neighboring grains are large. Based on this analysis, it is expected that the grain boundaries where the hydrogen concentration clearly increased in region B, which are indicated by black arrows in Fig. 5, consisted of two grains that had large differences in their Taylor factors. Therefore, it was likely that the number of vacancies increased significantly around these grain boundaries, and then hydrogen was repartitioned to the generated vacancies; thus, the hydrogen concentration increased at these grain boundaries.

3.4 Quasi-cleavage fracture and hydrogen accumulation

Accumulated hydrogen should be repartitioned to not only the generated vacancies but also to some trapping sites when the binding energy and trapping site density are high. It has been reported that the binding energies of the precipitate interface, Al_7Cu_2Fe particles, and micropore are higher than the value of vacancy through first-principles calculations.[23,24,26,27] Of these three trapping sites, since the precipitate have most dense distribution, it is thought that hydrogen is redistributed to the precipitate. Therefore, many precipitate interfaces existing near the specific grain boundaries, where the hydrogen concentration clearly increases, debonds. If more load was applied, it is likely that these micro cracks would connect, eventually forming the quasi-cleavage fracture.

4. Conclusion

By combining the KFM and tensile test results, the temporal changes in the hydrogen concentration of Al–Zn–Mg alloy under tensile stress were directly measured. The changes occurred especially along grain boundaries. The amplitude of the change in hydrogen concentration corresponded to the equivalent strain distribution, and hydrogen accumulated in the vicinity of the grain boundaries that existed in the high-strain region. The changes in the hydrogen concentration, which were measured under tensile strain, occurred due to hydrogen diffusion caused by the influence of hydrostatic stress, which acted as a driving force for diffusion, and by the hydrogen repartitioning behavior in the localized deformation region. Additionally, when hydrogen was accumulated to the localized deformation region, it was likely that hydrogen would be repartitioned to the precipitate interface, which had a high binding energy and most dense distribution, and that this hydrogen accumulation, then facilitated the occurrence of fracture.

Acknowledgments

This research was supported by Japan Science and Technology Agency (JST) under Collaborative Research Based on Industrial Demand “Heterogeneous Structure Control: Towards Innovative Development of Metallic Structural Materials”, Grant Number JPMJSK1412, Japan. The Kelvin force microscopy experiments were performed in the Kyushu University Cleanroom Laboratory Facility. The synchrotron radiation experiments were performed at the BL20XU of SPring-8 with the approval of Japan Synchrotron Radiation Research Institute (JASRI) (Proposal No. 2017B0076). This work was supported by JSPS KAKENHI Grant Number JP20J11740.

REFERENCES

1) T. Neeraj, R. Srinivasan and J. Li: Acta Mater. **60** (2012) 5160–5171.
2) Z. Zhang, G. Obasi, R. Morana and M. Preuss: Acta Mater. **113** (2016) 272–283.
3) Z. Zhang, G. Obasi, R. Morana and M. Preuss: Scr. Mater. **140** (2017) 40–44.
4) K. Hirayama, H. Toda, Y. Sek, T. Suzuki, M. Uesugi, A. Takeuchi and W. Ludwig: Mater. Trans., to be submitted.
5) T. Tsuru, K. Shimizu, M. Yamaguchi, M. Itakura, K. Ebihara, A. Bendo, K. Matsuda and H. Toda: Sci. Rep. **10** (2020) 1998.
6) H. Su, H. Toda, K. Shimizu, K. Uesugi, A. Takeuchi and Y. Watanabe: Acta Mater. **176** (2019) 96–108.
7) R. Koyama and G. Itoh: Trans. Nonferrous Met. Soc. China **24** (2014) 2102–2106.
8) K. Horikawa and K. Yoshida: J. Japan Inst. Met. **68** (2004) 1043–1046.
9) C. Larignon, J. Alexis, E. Andrieu, L. Lacroix, G. Odemer and C. Blanc: Electrochim. Acta **110** (2013) 484–490.
10) K. Takai, J. Seki and Y. Homma: Mater. Trans. JIM **36** (1995) 1134–1139.
11) Z. Tarzimoghadam, M. Rohwerder, S.V. Merzlikin, A. Bashir, L. Yedra, S. Eswara, D. Ponge and D. Raabe: Acta Mater. **109** (2016) 69–81.
12) J. Takahashi, K. Kawakami, Y. Kobayashi and T. Tarui: Scr. Mater. **63** (2010) 261–264.
13) C. Senöz, S. Evers, M. Stratmann and M. Rohwerder: Electrochem. Commun. **13** (2011) 1542–1545.
14) S. Evers and M. Rohwerder: Electrochem. Commun. **24** (2012) 85–88.
15) C. Larignon, J. Alexis, E. Andrieu, L. Lacroix, G. Odemer and C. Blanc: Scr. Mater. **68** (2013) 479–482.
16) M. Kobayashi, H. Toda, Y. Kawai, T. Ohgaki, K. Uesugi, D.S. Wilkinson, T. Kobayashi, Y. Aoki and M. Nakazawa: Acta Mater. **56** (2008) 2167–2181.
17) M.S. Bhuiyan, Y. Tada, H. Toda, S. Hang, K. Uesugi, A. Takeuchi, N. Sakaguchi and Y. Watanabe: Int. J. Fract. **200** (2016) 13–29.
18) M.F. Ashby: Philos. Mag. **21** (1970) 399–424.
19) S. Brinckmann, T. Siegmund and Y. Huang: Int. J. Plast. **22** (2006) 1784–1797.
20) J. Nye: Acta Metall. **1** (1953) 153–162.
21) M. Militzer, W.P. Sun and J.J. Jonas: Acta Metall. Mater. **42** (1994) 133–141.
22) K. Shimizu, H. Toda, C. Kadogawa, H. Fujihara and A. Takeuchi: Materialia **11** (2020) 100667.
23) M. Yamaguchi, M. Itakura, T. Tsuru and K. Ebihara: Mater. Trans. **62** (2021) 582–589.
24) L. Ismer, M.S. Park, A. Janotti and C.G. Van de Walle: Phys. Rev. B **80** (2009) 184110.
25) H. Toda, T. Kamiko, Y. Tanabe, M. Kobayashi, D.J. Leclere, K. Uesugi, A. Takeuchi and K. Hirayama: Acta Mater. **107** (2016) 310–324.
26) M. Yamaguchi, T. Tsuru, K. Ebihara and M. Itakura: J. JILM **68** (2018) 588–595.
27) M. Yamaguchi, T. Tsuru, K. Ebihara, M. Itakura, K. Matsuda, K. Shimizu and H. Toda: Mater. Trans. **61** (2020) 1907–1911.